CHEMISTRY

Semiconductor-metal transition powers high-efficiency MgAgSb thermoelectrics

Airan Li[1]†, Longquan Wang[1]†, Xinzhi Wu[1]†, Jiankang Li[1,2], Xinyuan Wang[1,2], Gang Wu[1], Zhao Hu[1,2], Takao Mori[1,2]*

Because of the inferior thermoelectric performance of metals, the semiconductor-to-metal transition in thermoelectric materials is always avoided. Here, we demonstrate that α-to-β semiconductor-metal transition in MgAgSb is actually not detrimental but can be strategically exploited to create α/β-MgAgSb junction, enabling 150% enhancement in output power while maintaining high conversion efficiency. This power enhancement lies in the notably reduced internal resistance induced by semiconductor-to-metal transition, which is independent of dimensional changes. Consequently, α/β-MgAgSb can simultaneously achieve high maximum conversion efficiency exceeding 10% (9%) and maximum power density above 1 (0.9) W cm^{-2} by simulation (experiment), outperforming most p-type materials under identical conditions. In addition, a two-pair thermoelectric module combining α/β-MgAgSb with n-type $Mg_3Sb_{0.6}Bi_{1.4}$ achieves an unprecedented power density, representing notable advancements over existing $Mg_3(Sb,Bi)_2$/MgAgSb two-pair system. These findings highlight the immense potential of α/β-MgAgSb for thermoelectric applications and provide insights into the design of high-power thermoelectrics.

INTRODUCTION

The increasing consumption of fossil fuels has led to vast amounts of carbon dioxide being released into the atmosphere, accompanied by notable waste heat generation. This not only exacerbates climate change but also poses a formidable challenge to achieving a carbon-neutral society. Addressing these issues necessitates innovative technologies capable of efficiently utilizing wasted energy resources. Thermoelectric (TE) technology, which directly converts heat into electricity without moving parts, represents a highly promising solution (*1*, *2*). In addition to waste heat power generation by harvesting heat from the environment, TE devices can provide a sustainable power source for electronic devices and numerous sensors, where decentralized and energy-efficient power systems are critical. This demands TE devices having both high conversion efficiency η and high power density ω (*3*, *4*).

Traditionally, the primary focus in TE research has been on achieving a high figure of merit zT of the material, as it is directly correlated with maximum conversion efficiency η_{max} of TE devices (*5*–*7*). zT is defined as $zT = S^2\sigma/\kappa \times T$, where S, σ, κ, and T represent the Seebeck coefficient, electrical conductivity, thermal conductivity, and absolute temperature, respectively. Over the past few decades, substantial progress has been made in developing multifunctional high-performance TE materials and strategies to enhance their zT (*8*–*11*). As a result, the η_{max} of state-of-the-art TE devices has reached ~7 to 10% near the room temperature range and 10 to 15% in the mid to high-temperature range (*12*–*18*).

While high η_{max} is critical, achieving high maximum power density ω_{max} is equally important for practical applications (*19*, *20*). High ω_{max} directly determines the output power capability and overall energy utilization rate of TE devices, making it indispensable for real-world applications. Enhancing the power factor (PF = $S^2\sigma$) of TE materials is vital for achieving high ω_{max}. The PF is determined by carrier transport behavior and can be improved through band structure engineering and carrier density optimization (*21*, *22*). However, while certain metals could exhibit high PF due to their excellent electrical properties, their inherently high κ poses a challenge in achieving high zT and, consequently, high η_{max} (*23*). Nonetheless, it should be mentioned that metals can often find a niche as TE interface materials (TEiMs), where high σ and κ are desirable to minimize energy loss during heat and electricity transport (*24*, *25*).

For typical TE materials, the intricate interplay among S, σ, and κ makes it particularly challenging to simultaneously achieve high S, high σ, and low κ, which are essential for achieving both high η_{max} and ω_{max}. Among the wide array of TE materials, Bi_2Te_3-based compounds stand out for their high PF and high zT at room temperature, making them the only TE materials commercialized, primarily for cooling applications (*26*–*28*). However, their use in power generation remains limited due to a notable decrease in zT above room temperature, resulting in relatively low η_{max}. This limitation is now being challenged by the emergence of n-type $Mg_3(Sb,Bi)_2$ and p-type MgAgSb (*29*, *30*). MgAgSb stands out as one of the most promising p-type TE materials for applications in the room temperature range, offering its excellent TE properties, air robustness, and eco-friendliness (*31*–*33*). Advancements such as phase purity control (*34*, *35*), doping optimization (*36*, *37*), global softening (*38*), and grain size regulation (*39*) have notably improved the zT of MgAgSb, reaching values between 1.0 and 1.6. In addition, the development of TEiMs has further accelerated its application in power generation (*24*, *29*, *40*, *41*). However, despite achieving η_{max} exceeding 7%, the ω_{max} of its corresponding TE modules remains low, requiring further enhancements to meet diverse power demands.

A unique feature of MgAgSb is its multiple phase transitions with temperature (*31*). Among these phases, only the semiconducting α-MgAgSb exhibits excellent TE performance, whereas both β-MgAgSb and γ-MgAgSb show much lower zT values (*42*). As a result, the application of MgAgSb is limited to its α-phase range. Notably, γ-MgAgSb is highly stable once formed, posing a major challenge to realizing the high performance of MgAgSb (*31*, *35*). In comparison,

---

[1] Research Center for Materials Nanoarchitectonics (MANA), National Institute for Materials Science (NIMS), Namiki 1-1, Tsukuba 305-0044 Japan. [2] Graduate School of Pure and Applied Sciences, University of Tsukuba, Tennodai 1-1-1, Tsukuba 305-8671 Japan.
*Corresponding author. Email: mori.takao@nims.go.jp
†These authors contributed equally to this work.

β-MgAgSb remains less extensively studied. Reports indicate that β-MgAgSb exhibits metallic behavior, characterized by high σ but low S and high κ (*31*). These properties result in a low zT for β-MgAgSb, rendering it undesirable in MgAgSb-based applications. Consequently, the α-to-β semiconductor-metal transition is typically avoided to prevent the introduction of the low-zT β-MgAgSb, limiting the operation temperature of MgAgSb-based TE devices below 573 to 593 K (*29*).

In this work, contrary to previous understanding, we demonstrate that the α-to-β phase transition in MgAgSb can be leveraged to enhance the performance of MgAgSb-based TE devices. This semiconductor-metal transition allows the creation of an α/β-MgAgSb junction, which not only maintains high efficiency but also achieves a notable 150% increase in output power compared to pristine α-MgAgSb. Simulation (and experiment) show that α/β-MgAgSb can achieve η_{max} exceeding 10% (9%) and ω_{max} above 1 (0.9) W cm^{-2}, outperforming other representative p-type TE materials under identical conditions. We investigate the α-to-β phase transition and find that α-MgAgSb can transform into β-MgAgSb and revert between room temperature and 623 K, with β-MgAgSb demonstrating exceptional stability, enabling continuous power generation without degradation even at 623 K. We then fabricate two-pair TE modules with MgAgSb and n-type $Mg_3(Sb,Bi)_2$. The MgAgSb/$Mg_3Sb_{0.6}Bi_{1.4}$ two-pair module achieves η_{max} of 8.6% and record-high ω_{max} of 0.5 W cm^{-2} (10 by 10 mm^2 base), advancing existing MgAgSb/$Mg_3(Sb,Bi)_2$ modules. This work underscores the potential of MgAgSb for efficient power generation and provides valuable insights for designing future high-performance TEs with both high output power and high efficiency.

RESULTS

Semiconducting α-MgAgSb and metallic β-MgAgSb

MgAgSb exhibits three distinct phases: α-MgAgSb, β-MgAgSb, and γ-MgAgSb (*31*). With increasing temperature, α-MgAgSb transitions to β-MgAgSb first. As shown in Fig. 1A, both α-MgAgSb and β-MgAgSb share a tetragonal crystal structure but differ in their

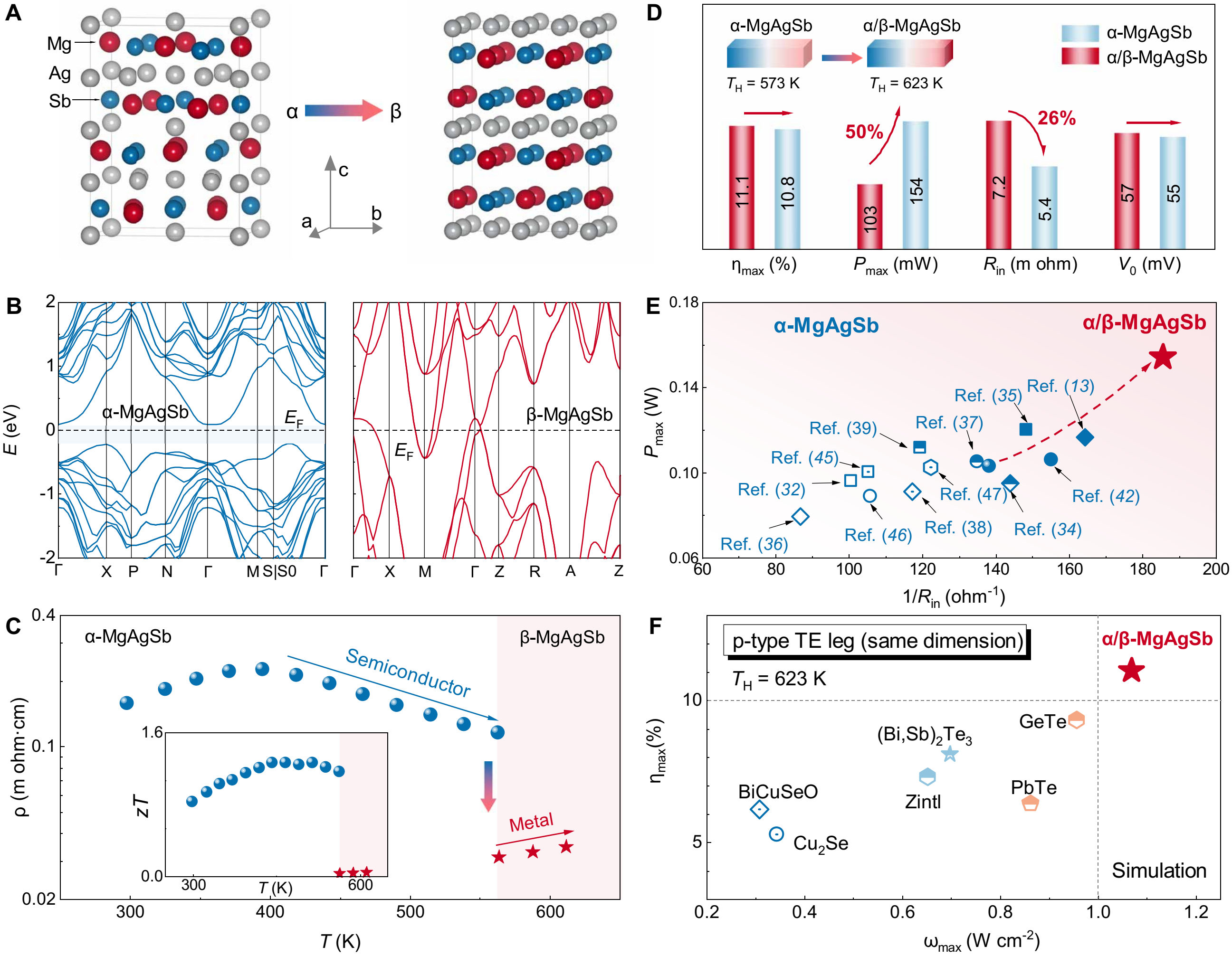

Fig. 1. Semiconducting α-MgAgSb and metallic β-MgAgSb. (**A**) Crystal structure of semiconducting α-MgAgSb and metallic β-MgAgSb. (**B**) Band structures of α-MgAgSb and β-MgAgSb. (**C**) T-dependent ρ for α-MgAgSb and β-MgAgSb, with the inset showing their corresponding T-dependent zT values. (**D**) Simulated η_{max}, P_{max}, R_{in}, and V_0 for α-MgAgSb and α/β-MgAgSb single TE legs. The inset is the schematic diagram of the α-MgAgSb leg and α/β-MgAgSb junction leg when T_H = 573 and 623 K, respectively. (**E**) Comparison of simulated $1/R_{in}$ versus P_{max} of α-MgAgSb and α/β-MgAgSb in this work with the literature (*13*, *32*, *34*–*39*, *42*, *45*–*47*). (**F**) Comparison of simulated η_{max} versus ω_{max} of α/β-MgAgSb with representative p-type TE materials, including $(Bi,Sb)_2Te_3$ (*48*), GeTe (*15*), PbTe (*49*), Zintl (*18*), BiCuSeO (*50*), and Cu_2Se (*51*).

space groups: α-MgAgSb belongs to *I*-4*c*2, while β-MgAgSb adopts *P*4/*nmm*. Previous studies suggest that the α-to-β phase transition is driven by Ag atom rearrangement, which induces a semiconductor-to-metal transition in MgAgSb (*43*). Specifically, α-MgAgSb is a typical semiconductor with a bandgap of ~0.18 eV, while β-MgAgSb, as a metal, lacks a bandgap (Fig. 1B). The temperature dependence of resistivity ρ further confirms this behavior: α-MgAgSb shows semiconductive characteristics, with its ρ decreasing due to bipolar conduction, whereas β-MgAgSb exhibits metallic transport behavior, as indicated by its increasing ρ with temperature (Fig. 1C). Generally, metals have high carrier concentrations, resulting in a very high σ (low ρ) but a very low *S*. In addition, the high σ of metals typically leads to high κ according to Wiedemann-Franz law, resulting in low zT values. Figure S1 displays the σ, *S*, and κ of MgAgSb. Because of its low *S* and high κ, the metallic β-MgAgSb has a much lower zT compared to the semiconducting α-MgAgSb, as shown in the inset of Fig. 1C.

For a long time, the α-to-β semiconductor-metal transition was avoided to prevent the formation of β-MgAgSb due to its low zT. However, changing the viewpoint, the metallic nature of β-MgAgSb can actually make it a promising candidate as a TEiM, especially when used alongside α-MgAgSb to form an α/β-MgAgSb junction. Unlike previous junctions made from different materials with different compositions, this junction is formed by materials with the same composition but two different crystallographic phases, which may help mitigate atomic diffusion. A simple method to create the α/β-MgAgSb junction is by increasing the hot-side temperature T_H. When the T_H of α-MgAgSb rises to 623 K, an α/β-MgAgSb junction forms naturally, as shown in the inset of Fig. 1D. Compared to α-MgAgSb at $T_H = 573$ K, the increase in the temperature gradient ($\Delta T = T_H - T_C$, where T_C is the cold-side temperature) could benefit both the η_{max} and the maximum output power P_{max}, as both are positively correlated with ΔT (*44*).

However, the emergence of β-MgAgSb also alters the overall TE properties of MgAgSb. The potential increase in η_{max} may be offset by a reduced average figure of merit zT_{avg}, but the P_{max} may be notably enhanced due to the semiconductor-metal transition. To accurately assess the performance of the α/β-MgAgSb junction, finite-element analysis was used. As shown in Fig. 1D, although the η_{max} of α/β-MgAgSb is slightly reduced, it remains comparable to that of α-MgAgSb (97%). Crucially, P_{max} is notably enhanced (~150%) owing to the reduced internal resistance R_{in} induced by the α-to-β semiconductor-metal transition. Moreover, it should be noted that open-circuit V_0 remains nearly identical for both α-MgAgSb and α/β-MgAgSb. This highlights the pivotal role of the semiconductor-metal transition in minimizing R_{in}, thereby notably improving the P_{max}. In addition to electrical benefits, the metallic nature and high κ of β-MgAgSb may also help buffer against temperature fluctuations, a critical factor for the practical deployment of MgAgSb-based TE modules.

It is crucial to emphasize that the enhancement in P_{max} results from the decreased R_{in} is similar but different from modifying the physical dimensions of the TE leg. On one hand, the emergence of the β-MgAgSb phase partially replaces the original α-MgAgSb, effectively shortening the length of α-phase. At the same time, because of the metallic nature of β-MgAgSb, this substitution substantially reduces the internal resistance, thereby enhancing the output power. On the other hand, unlike conventional approaches that increase P_{max} by adjusting the TE leg's height or cross-sectional area, the improvement achieved through the α-to-β semiconductor-metal transition is independent of dimensional changes. As shown in figs. S2 to S3, regardless of variations in the TE leg's height or area, once the α/β-MgAgSb junction forms, an ~150% increase in P_{max} can be achieved while maintaining η_{max}. This further emphasizes the intrinsic ability of the α-to-β transition to reduce R_{in} and enhance power output. Detailed simulated current *I* dependence of output voltage *V*, heat flow, *Q* output power *P*, and conversion efficiency η for single MgAgSb TE legs with varying dimensions are provided in figs. S4 to S8.

Contrary to previous understanding, it is evident that the emergence of β-MgAgSb is not detrimental; instead, it presents an opportunity to substantially enhance the output power. To further demonstrate the benefits of α-to-β semiconductor-metal transition in MgAgSb, we simulated the R_{in} and P_{max} of various α-MgAgSb reported in literature (*2*, *13*, *32*, *34*–*39*, *45*–*47*) under identical dimensions (3.8 mm by 3.8 mm by 6 mm). The detailed *I*-dependent *V* and *P* are provided in figs. S9 to S12. Figure 1E summarizes the relationship between $1/R_{in}$ and P_{max} of a single MgAgSb TE leg in this work compared to literature (*2*, *13*, *32*, *34*–*39*, *45*–*47*). The results demonstrate that the α-to-β transition enables the α/β-MgAgSb junction to achieve a lower R_{in} and record-high P_{max}, underscoring the superior potential of α/β-MgAgSb over α-MgAgSb alone.

In terms of both η_{max} and ω_{max}, α/β-MgAgSb can simultaneously achieve a high η_{max} exceeding 10% and ω_{max} above 1 W cm^{-2}. To benchmark its performance, we compared α/β-MgAgSb with other representative p-type TE materials by simulation, including $(Bi,Sb)_2Te_3$ (*48*), GeTe (*15*), PbTe (*49*), Zintl (*18*), BiCuSeO (*50*), and Cu_2Se (*51*), under identical conditions (TE leg dimensions: 3.8 mm by 3.8 mm by 6 mm; $T_H = 623$ K). The detailed *I*-dependent *V*, *P*, *Q*, and η characteristics of these materials are shown in figs. S13 to S18, and Fig. 1F summarizes the η_{max} versus ω_{max}. It can be seen that α/β-MgAgSb exhibits excellent η_{max} and ω_{max} compared to others, further demonstrating its strong potential for applications.

α-to-β phase transition

Despite the promising potential of α/β-MgAgSb, the formation and stability of β-MgAgSb require thorough investigation for its practical applications. The α-to-β phase transition was studied first. As shown in Fig. 2A, the x-ray diffraction (XRD) patterns of MgAgSb during heating reveal that the phase remains indexed to α-MgAgSb at 573 K. However, upon reaching 623 K, β-MgAgSb begins to emerge. In addition, minor amounts of Sb and Ag_3Sb impurities appear during heating, consistent with previous reports (*31*, *52*, *53*). Once β-MgAgSb forms, it persists at 573 K during cooling but reverts to α-MgAgSb when the temperature is further reduced to 523 K, as depicted in Fig. 2B. A hysteresis phenomenon is observed between the α-to-β and β-to-α phase transitions. This hysteresis in phase transition temperature is also reflected in the TE transport properties, including *S*, σ, and κ, as shown in Fig. 2C and Fig. 2E, respectively. Notably, when β-MgAgSb reverts to α-MgAgSb, the TE properties nearly return to their original values, indicating good reversibility between α and β-phase. In contrast, for γ-MgAgSb, once it forms, it will persist even at room temperature, adversely affecting the performance of α-MgAgSb (*52*). However, β-MgAgSb can revert to α-MgAgSb without notably compromising its performance despite the persistence of trace Sb and Ag_3Sb impurities upon cooling (Fig. 2B).

The good reversibility between α-MgAgSb and β-MgAgSb also reflects the good stability of MgAgSb, which can be further supported

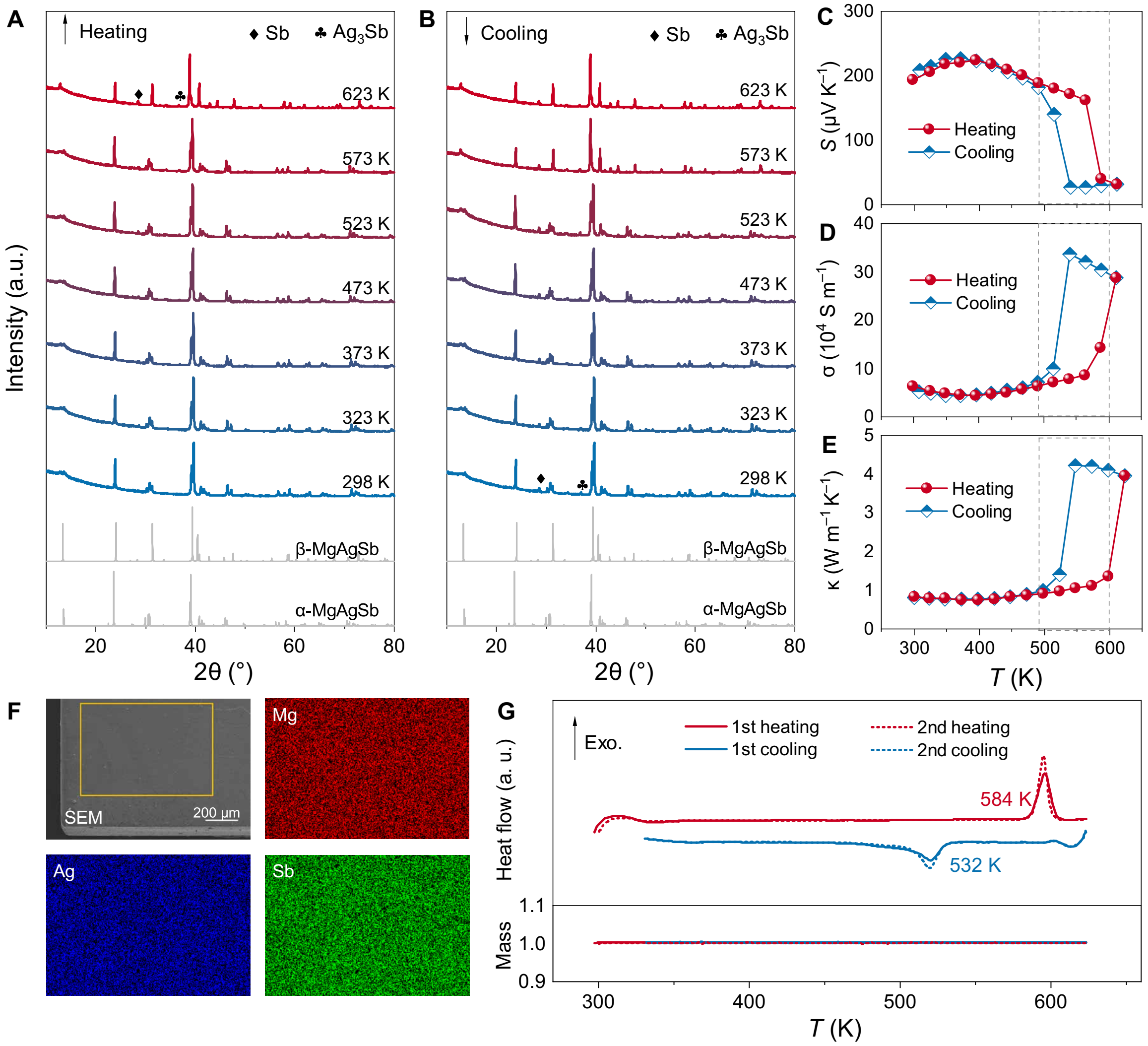

Fig. 2. Reversible and repeatable α-to-β phase transition. *T*-dependent XRD patterns of MgAgSb during (**A**) heating and (**B**) cooling, showing the reversible α-to-β and β-to-α phase transitions. *T* dependence of (**C**) *S*, (**D**) σ, and (**E**) κ of MgAgSb during heating and cooling within room temperature and 623 K. (**F**) Scanning electron microscopy (SEM) image and EDS mappings of Mg, Ag, and Sb in MgAgSb after a complete heating and cooling cycle. (**G**) TG-DSC curves of MgAgSb during the first and second heating and cooling tests. a.u., arbitrary unit.

by the homogeneous elemental distribution of Mg, Ag, and Sb revealed by energy dispersive x-ray spectroscopy (EDS) mappings after the heating and cooling (Fig. 2F). Furthermore, Fig. 2 (G and H) shows the thermogravimetric–differential scanning calorimetry (TG-DSC) curves of MgAgSb, which illustrate the reversible phase transitions between α-MgAgSb and β-MgAgSb, along with the corresponding mass changes. No mass changes were detected after heating and cooling, further confirming the good stability of MgAgSb with heating and cooling. This robustness is also evident in the subsequent heating and cooling cycle, where identical endothermic and exothermic peak positions were observed, and no mass variations were detected. This highlights the suitability of MgAgSb for practical applications, even with the α-to-β phase transition.

Highly stable β-MgAgSb

Although the phase transition between α-MgAgSb and β-MgAgSb is reversible and repeatable, the long-term thermal stability of β-MgAgSb is crucial for practical applications. As shown in Fig. 3A, repeated measurements of *S* and σ for β-MgAgSb over six cycles are consistent. Furthermore, extended stability tests at 623 K show no noticeable degradation, with the normalized values of σ/σ_0 and S/S_0 remaining around 1.0 (Fig. 3B). This demonstrates the outstanding thermal stability of β-MgAgSb, even at temperatures higher than the 573 K used for α-MgAgSb, making it highly suitable for long-term applications. It is also worth noting that although small amounts of Sb and Ag_3Sb form during heating, their metallic nature and low concentrations have minimal impact on the stability and metallic transport properties of β-MgAgSb.

To further demonstrate its potential, a MgAgSb single TE leg was fabricated, with the cold-side temperature fixed at 293 K, while the hot-side temperature was varied at 373, 473, 573, and 623 K. Figure S19 shows the corresponding measured *I* dependence of *V*, *P*, *Q*, and η. When the T_H reached 623 K, β-MgAgSb naturally and in situ formed, bonding with α-MgAgSb. As shown in Fig. 3C, the η_{max} of

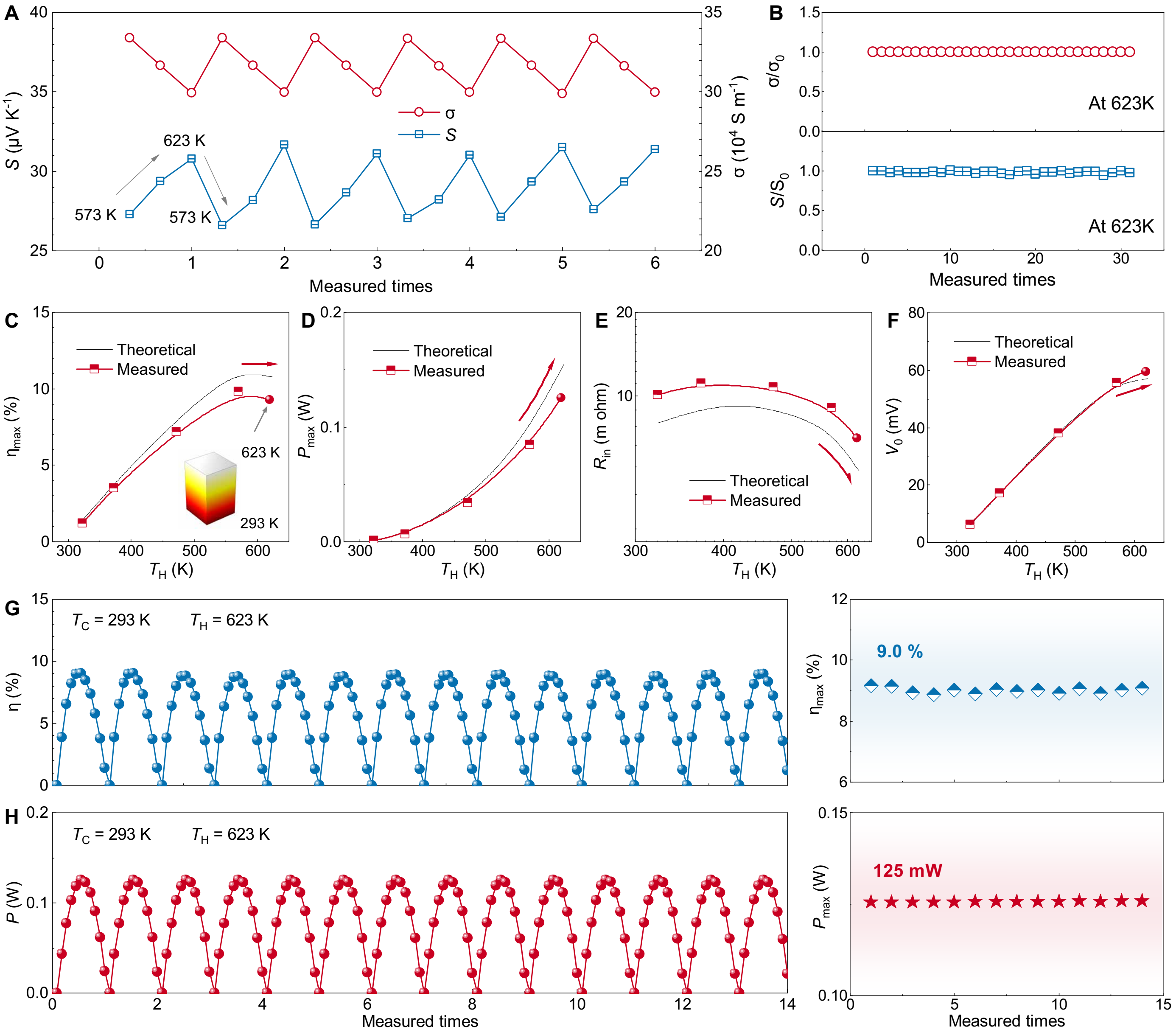

Fig. 3. Stability of β-MgAgSb and α/β-MgAgSb single TE leg. (**A**) T dependence of S and σ of β-MgAgSb over six repeated measurements. (**B**) Ratios of σ/σ_0 and S/S_0 for β-MgAgSb during multiple measurements at 623 K. T_H dependence of measured and theoretical (**C**) η_{max}, (**D**) P_{max}, (**E**) R_{in}, and (**F**) V_0 of MgAgSb single TE leg. Measured (**G**) η, η_{max} and (**H**) P, P_{max} of MgAgSb single TE leg under multiple measurements with a set T_H of 623 K and T_C of 293 K.

the α-MgAgSb TE leg at 573 K is 9.2%, while for the α/β-MgAgSb TE leg at 623 K, η_{max} slightly decreased to 9.0% due to the reduced overall zT value. The trend of the measured results aligns well with theoretical predictions, although slightly lower.

As discussed earlier, the α-to-β semiconductor-metal transition enables the α/β-MgAgSb junction to achieve a low R_{in} and record-high P_{max}. This improvement can further be seen in Fig. 3D, where the P_{max} of the α/β-MgAgSb TE leg is notably higher than that of the α-MgAgSb TE leg. In addition, Fig. 3 E and F shows a substantial reduction in R_{in} and a slight increase V_0 for α/β-MgAgSb (623 K) compared to α-MgAgSb (573 K). It is worth noting that the previous simulation did not account for the contact resistance between α- and β-MgAgSb. The agreement between experimental and simulated results in Fig. 3E suggests that the contact resistance between α-MgAgSb and β-MgAgSb is minimal. Furthermore, the metallic nature of β-MgAgSb also ensures good electrical contact with the electrode. These findings highlight the excellent reliability and performance of α/β-MgAgSb, offering low R_{in}, high η_{max}, and enhanced P_{max}. The stability of the α/β-MgAgSb TE leg was further evaluated through multiple measurement cycles at a set T_H of 623 K and T_C of 293 K. As shown in Fig. 3 (G and H), the α/β-MgAgSb TE leg consistently maintained its high η_{max}, and its P_{max} remained stable over repeated cycles. This high stability can be attributed to the exceptional thermal stability of β-MgAgSb at elevated temperatures, ensuring the reliable performance of α/β-MgAgSb for practical TE applications. In addition to the intrinsic stability of the material, the close similarity in thermal expansion between α-MgAgSb and β-MgAgSb also plays an important role in preserving the mechanical integrity of the leg (fig. S20). Moreover, the uniform elemental distribution across the α/β-MgAgSb leg after repeated tests further confirms the good stability of α/β-MgAgSb (fig. S21).

Besides, we also examined the post-test microstructure of α/β-MgAgSb (fig. S22). Hot and cold sides of α/β-MgAgSb exhibit similar transgranular fracture patterns with small intragrain pores. Notably, the fracture surface at hot side reveals notably larger grains, consistent with thermally driven grain growth at ~573 K reported previously (*39*). This grain growth can help reduce charge carrier and phonon scattering, thereby potentially improving the σ and κ of β-MgAgSb. These findings further confirm the effective role of β-MgAgSb when applied at high temperatures above 593 K. To our knowledge, this finding also enables the MgAgSb constituent device to be used above 593 K for the first time, unlocking possibilities for efficient waste heat recovery in steelworks.

Excellent power generation employing β-MgAgSb

The boosted P_{max}, maintained η_{max}, and demonstrated high stability of α/β-MgAgSb highlight its strong potential for practical applications. Typically, TE devices are composed of both n-type and p-type TE legs. In this study, p-type MgAgSb is coupled with n-type $Mg_3(Sb,Bi)_2$ to fabricate two-pair modules. To fully demonstrate the advantages of α/β-MgAgSb, two types of two-pair modules were assembled: one using Bi-rich $Mg_3Sb_{0.6}Bi_{1.4}$ and the other using Sb-rich $Mg_3Sb_{1.5}Bi_{0.5}$. Figure 4 (A and B) illustrates the I dependence of η and P, respectively, in Bi-rich $Mg_3Sb_{0.6}Bi_{1.4}$/MgAgSb two-pair module, with I dependence of V and Q shown in fig. S23. Similarly, when β-MgAgSb forms at the hot side of α-MgAgSb ($T_H = 623$ K), both maintained η_{max} and improved P_{max} are observed compared to α-MgAgSb alone ($T_H = 573$ K). Moreover, when the operating temperature exceeds the α-β transition point of MgAgSb, the effective temperature gradient across the n-type $Mg_3Sb_{0.6}Bi_{1.4}$ leg also increases, further enhancing the overall power output and conversion efficiency of the device. Similar results are also evident in modules using Sb-rich $Mg_3Sb_{1.5}Bi_{0.5}$ (Fig. 4, C and D, and fig. S24). These findings further strengthen the capability of α/β-MgAgSb to enhance P while maintaining high η. Figure 4E summarizes the ratios of η_{max} and P_{max} in single-leg and two-pair modules using α-MgAgSb and α/β-MgAgSb. This comparison further emphasizes that α/β-MgAgSb can achieve a similar η_{max} to α-MgAgSb while delivering notably enhanced P_{max}.

Figure 4F shows the ΔT dependence of η_{max} in the two-pair $Mg_3(Sb,Bi)_2$/MgAgSb modules, alongside comparisons to values reported in the literature (*14*, *24*, *30*, *38*, *40*, *54*–*58*). The high η_{max} of 8.6% achieved in the $Mg_3Sb_{0.6}Bi_{1.4}$/MgAgSb module is comparable to the best-reported results. As shown in Fig. 4G, the $Mg_3Sb_{0.6}Bi_{1.4}$/MgAgSb module achieves a record-breaking ω_{max} of 0.5 W cm^{-2}, outperforming other modules (*14*, *24*, *30*, *38*, *40*, *54*–*58*). Figure 4H illustrates the relationship between η_{max} versus ω_{max}, and it can be found the two-pair TE module using α/β-MgAgSb as the p-type TE legs and $Mg_3Sb_{0.6}Bi_{1.4}$ as the n-type TE legs not only achieves a higher ω_{max} but also maintains a high η_{max} compared to one using α-MgAgSb. Its performance is particularly noteworthy among $Mg(Sb,Bi)_2$/MgAgSb two-pair modules offering both high ω_{max} and high η_{max} (*14*, *24*, *30*, *38*, *40*, *54*–*58*). It should be emphasized that ω_{max} is calculated based on $\omega_{max} = P_{max}/A$, where A represents the total cross-sectional area of the TE device. The total cross-sectional area used here is the area of the ceramic base (10 mm by 10 mm). If the cross-sectional area of TE legs (3.8 mm by 3.8 mm × 2 pairs) is used, then ω_{max} would be 0.9 W cm^{-2}. These results highlight the notable potential of α/β-MgAgSb to replace α-MgAgSb. The integration of β-MgAgSb within α-MgAgSb is anticipated to expand its applicability across various TE systems.

DISCUSSION

In this study, we systematically investigated the reversible and repeatable α-to-β semiconductor-metal transition in MgAgSb. We demonstrated that α-MgAgSb, with a semiconductive nature, transitions to metallic β-MgAgSb at elevated temperatures. Although the β-MgAgSb exhibits lower zT values, its metallic nature makes it promising to couple with α-MgAgSb to form a nondiffusive α/β-MgAgSb junction. The incorporation of β-MgAgSb in the α/β-MgAgSb junction notably enhances its power output without sacrificing conversion efficiency, verified both theoretically and experimentally. Notably, the α/β-MgAgSb leg demonstrated excellent thermal stability during repeated tests, with no observable degradation of output performance. To further leverage α/β-MgAgSb, two-pair modules are fabricated, pairing with n-type Bi-rich $Mg_3Sb_{0.6}Bi_{1.4}$ or Sb-rich $Mg_3Sb_{1.5}Bi_{0.5}$. $Mg_3Sb_{0.6}Bi_{1.4}$ and α/β-MgAgSb module achieves η_{max} of 8.6% and reaches a record-breaking ω_{max} of 0.51 W cm^{-2}, highlighting their superior performance compared to conventional $Mg_3(Sb,Bi)_2$/MgAgSb two-pair systems. These findings not only demonstrate the feasibility of α/β-MgAgSb for high-performance TE systems but also pave the way for exploring similar phase transition–based TE materials and devices in the future.

MATERIALS AND METHODS

Materials synthesis

MgAgSb containing 0.625 wt% $C_{18}H_{36}O_2$ (referred to as MgAgSb in the main text and below), $Mg_{3.2}In_{0.02}Sb_{0.595}Bi_{1.4}Te_{0.005}$ (referred to as $Mg_3Sb_{0.6}Bi_{1.4}$ in the main text and below), and $Mg_{3.2}In_{0.005}Sb_{1.5}Bi_{0.49}Te_{0.01}$ (referred to as $Mg_3Sb_{1.5}Bi_{0.5}$ in the main text and below) were prepared using high-purity Mg turnings (99.95%), Ag powders (99.99%), Sb shots (99.999%), Bi shots (99.999%), Te shots (99.999%), and In powders (99.99%). Raw materials were weighed according to their stoichiometric ratios and mechanically alloyed for 5 hours using a SPEX-8000D mill under an argon atmosphere. The resulting powders were consolidated into bulk samples via vacuum spark plasma sintering. MgAgSb was sintered at 573 K and 60 MPa for 5 min (SPS-322Lx, Dr. Sintering), while $Mg_3Sb_{0.6}Bi_{1.4}$ and $Mg_3Sb_{1.5}Bi_{0.5}$ were sintered at 973 K and 60 MPa for 10 min (SPS-1080 System, SPS SYNTEX INC).

Characterization and measurements

The phase and phase transitions of MgAgSb were investigated using a variable-temperature x-ray diffractometer (Rigaku SmartLab 9 kW) with Cu K_α radiation at 45 kV and 200 mA. The measurements were performed on MgAgSb powders as the temperature increased from room temperature to 623 K and then cooled back to room temperature at a rate of 5 K min^{-1} under a dry N_2 gas flow of 2 liter min^{-1}. The electrical transport properties of MgAgSb, including S and the σ, were measured by ZEM-3 (Advance Riko) with ±5% uncertainty. The thermal transport property κ of MgAgSb was obtained by multiplying thermal diffusivity D via LFA467 (Netzsch), sample density ρvia Archimedes method, and heat capacity C_p via Dulong-Petit law. The thermal analysis TG-DSC of MgAgSb was performed using a

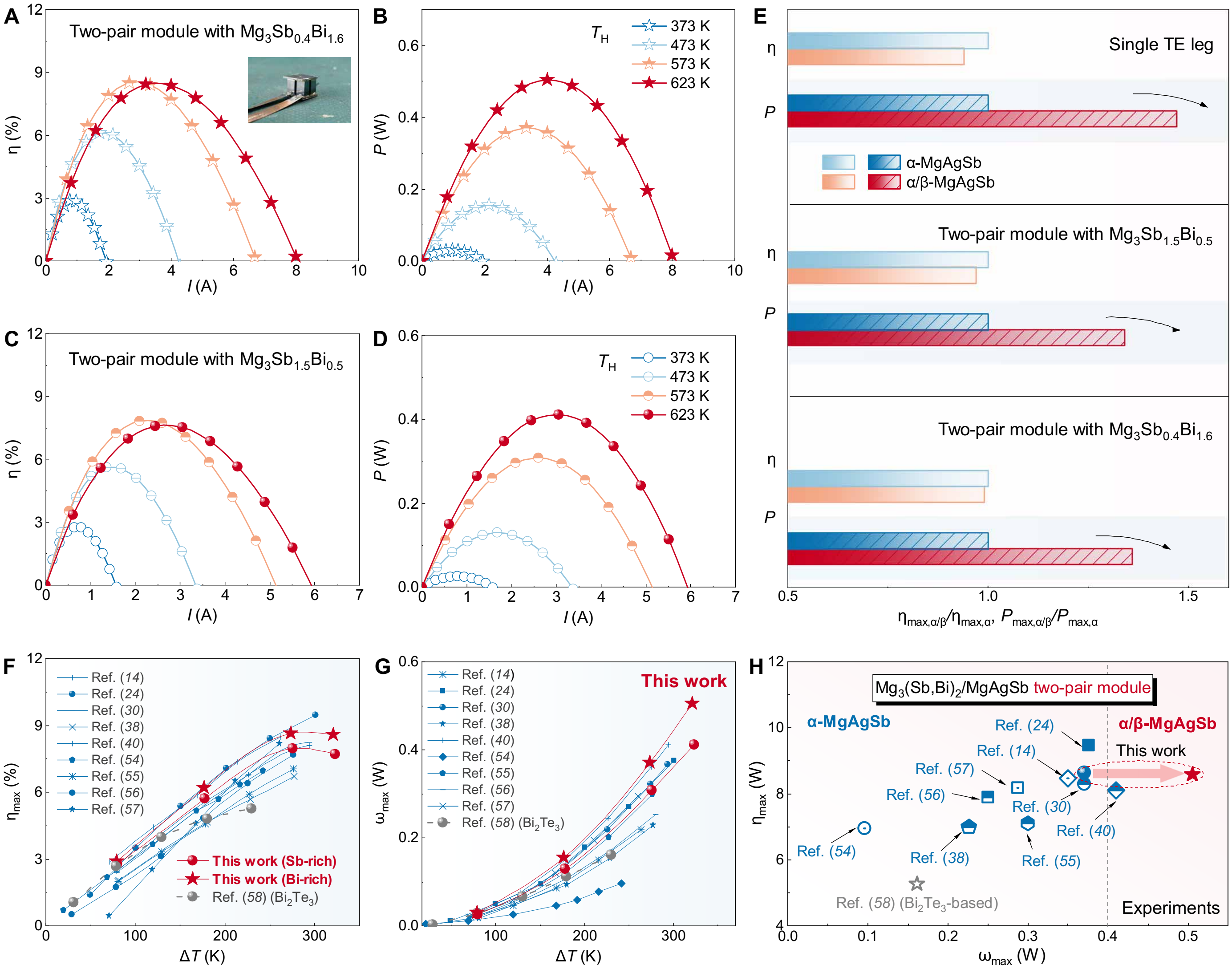

Fig. 4. Two-pair TE modules based on n-type $Mg_3(Sb,Bi)_2$ and p-type MgAgSb. *I* dependence of (**A**) η and (**B**) *P* in Bi-rich $Mg_3Sb_{0.6}Bi_{1.4}$/MgAgSb two-pair module, (**C**) η and (**D**) *P* in Sb-rich $Mg_3Sb_{1.5}Bi_{0.5}$/MgAgSb two-pair module. (**E**) Summary of the ratios of η_{max} and P_{max} for single TE leg and two-pair TE modules using α-MgAgSb and α/β-MgAgSb. Δ*T* dependence of the (**F**) η_{max} and (**G**) ω_{max} achieved in this study compared to values reported in the literature. (**H**) Comparison of η_{max} and ω_{max} of the $Mg_3(Sb,Bi)_2$/MgAgSb two-pair module in this work with values reported in the literature (*14*, *24*, *30*, *38*, *40*, *54*–*58*).

STA 449 (Netzsch). Samples were loaded into aluminum crucibles, heated to 623 K, and then cooled to 323 K at a rate of 5 K min^{-1}. The composition distribution of MgAgSb after the heating and cooling cycle was examined using field-emission scanning electron microscopy (Hitachi SU8000) equipped with an energy-dispersive spectrometer (EDS, XFlash FlatQUAD 5060 F).

TE device fabrication, measurement, and simulation

The MgAgSb TE leg was fabricated by sandwiching two layers of Sb powders as interface materials, followed by SPS (SPS-322Lx, Dr. Sintering) at 573 K and 60 MPa for 5 min. The sintered MgAgSb TE legs were then cut into dice with dimensions of ~3.8 mm by 3.8 mm by 6 mm. When the hot-side temperature was below 573 K, the MgAgSb leg remained in the α-MgAgSb phase, while at 623 K, it transitioned to the α/β-MgAgSb phase. Two-pair TE modules were constructed using these p-type MgAgSb legs and n-type Bi-rich $Mg_3Sb_{0.6}Bi_{1.4}$ or Sb-rich $Mg_3Sb_{1.5}Bi_{0.5}$ TE legs, with 304 stainless steel serving as the TEiM. The dimensions of the two-pair TE modules are 10 mm by 10 mm by 7.67 mm, with the height of the TE legs, AlN ceramic plate, and copper electrode being 6, 0.635, and 0.2 mm, respectively. The output power *P* and heat flow *Q* of both the single-leg and two-pair TE devices were measured using Mini-PEM (Advance Riko) in a vacuum. The conversion efficiency η was calculated based on the formula: $\eta = P/(P + Q)$. Finite-element simulations were performed using COMSOL Multiphysics to model both the single-leg and two-pair TE devices.

First-principles calculations

The band structure of α-MgAgSb and β-MgAgSb was calculated by using Vienna ab initio Simulation Package (VASP) software (*59*, *60*). Generalized gradient approximation - Perdew-Burke-Ernzerhof type was used and modified Becke-Johnson (mBJ) exchange-correlation functionals to get more accurate bandgap of MgAgSb (*61*, *62*). Geometry relaxation was conducted first to get the relaxed structure of α-MgAgSb and β-MgAgSb for the next self-consistent static calculations. The plane-wave energy cutoff was set to 500 eV. Hellmann-Feynman force on each atom energy was set to 0.001 eV $Å^{-1}$, and the convergence criterion was set to 10^{-8} eV. For geometry relaxation and self-consistent static calculations, $k = 30/L$ and $k = 60/L$ gamma-centered k-point sampling were adopted, respectively, where the L is the lattice parameter of MgAgSb. The calculated data were post-processed with the aid of VASPKIT (*63*) to obtain the band structures of α-MgAgSb and β-MgAgSb.

Supplementary Materials

This PDF file includes:

Figs. S1 to S24

REFERENCES AND NOTES

1. G. J. Snyder, E. S. Toberer, Complex thermoelectric materials. *Nat. Mater.* **7**, 105–114 (2008).
2. J. He, T. M. Tritt, Advances in thermoelectric materials research: Looking back and moving forward. *Science* **357**, eaak9997 (2017).
3. I. Petsagkourakis, K. Tybrandt, X. Crispin, I. Ohkubo, N. Satoh, T. Mori, Thermoelectric materials and applications for energy harvesting power generation. *Sci. Technol. Adv. Mater.* **19**, 836–862 (2018).
4. Q. Yan, M. G. Kanatzidis, High-performance thermoelectrics and challenges for practical devices. *Nat. Mater.* **21**, 503–513 (2022).
5. T. Zhu, Y. Liu, C. Fu, J. P. Heremans, J. G. Snyder, X. Zhao, Compromise and synergy in high-efficiency thermoelectric materials. *Adv. Mater.* **29**, 1605884 (2017).
6. T. Mori, Novel principles and nanostructuring methods for enhanced thermoelectrics. *Small* **13**, 1702013 (2017).
7. Y. Xiao, L.-D. Zhao, Seeking new, highly effective thermoelectrics. *Science* **367**, 1196–1197 (2020).
8. S. Roychowdhury, T. Ghosh, R. Arora, M. Samanta, L. Xie, N. K. Singh, A. Soni, J. He, U. V. Waghmare, K. Biswas, Enhanced atomic ordering leads to high thermoelectric performance in $AgSbTe_2$. *Science* **371**, 722–727 (2021).
9. Y. Wang, A. Li, Y. Hong, T. Deng, P. Deng, Y. Huang, K. Liu, J. Wang, C. Fu, T. Zhu, Iterative sublattice amorphization facilitates exceptional processability in inorganic semiconductors. *Nat. Mater.*, 10.1038/s41563-024-02112-7 , (2025).
10. S. Liu, S. Bai, Y. Wen, J. Lou, Y. Jiang, Y. Zhu, D. Liu, Y. Li, H. Shi, S. Liu, L. Wang, J. Zheng, Z. Zhao, Y. Qin, Z. Liu, X. Gao, B. Qin, C. Chang, C. Chang, L.-D. Zhao, Quadruple-band synglisis enables high thermoelectric efficiency in earth-abundant tin sulfide crystals. *Science* **387**, 202–208 (2025).
11. S. Xu, S. Horta, A. Lawal, K. Maji, M. Lorion, M. Ibáñez, Interfacial bonding enhances thermoelectric cooling in 3D-printed materials. *Science* **387**, 845–850 (2025).
12. C. Fu, S. Bai, Y. Liu, Y. Tang, L. Chen, X. Zhao, T. Zhu, Realizing high figure of merit in heavy-band p-type half-Heusler thermoelectric materials. *Nat. Commun.* **6**, 8144 (2015).
13. Z. Liu, N. Sato, W. Gao, K. Yubuta, N. Kawamoto, M. Mitome, K. Kurashima, Y. Owada, K. Nagase, C.-H. Lee, J. Yi, K. Tsuchiya, T. Mori, Demonstration of ultrahigh thermoelectric efficiency of ∼7.3% in Mg_3Sb_2/MgAgSb module for low-temperature energy harvesting. *Joule* **5**, 1196–1208 (2021).
14. P. Ying, L. Wilkens, H. Reith, N. P. Rodriguez, X. Hong, Q. Lu, C. Hess, K. Nielsch, R. He, A robust thermoelectric module based on MgAgSb/$Mg_3(Sb,Bi)_2$ with a conversion efficiency of 8.5% and a maximum cooling of 72 K. *Energ. Environ. Sci.* **15**, 2557–2566 (2022).
15. L. Xie, C. Ming, Q. Song, C. Wang, J. Liao, L. Wang, C. Zhu, F. Xu, Y.-Y. Sun, S. Bai, L. Chen, Lead-free and scalable GeTe-based thermoelectric module with an efficiency of 12%. *Sci. Adv.* **9**, eadg7919 (2023).
16. D. Liu, D. Wang, T. Hong, Z. Wang, Y. Wang, Y. Qin, L. Su, T. Yang, X. Gao, Z. Ge, B. Qin, L.-D. Zhao, Lattice plainification advances highly effective SnSe crystalline thermoelectrics. *Science* **380**, 841–846 (2023).
17. H. Hu, Y. Ju, J. Yu, Z. Wang, J. Pei, H.-C. Thong, J.-W. Li, B. Cai, F. Liu, Z. Han, B. Su, H.-L. Zhuang, Y. Jiang, H. Li, Q. Li, H. Zhao, B.-P. Zhang, J. Zhu, J.-F. Li, Highly stabilized and efficient thermoelectric copper selenide. *Nat. Mater.* **23**, 527–534 (2024).
18. X. Shi, S. Song, G. Gao, Z. Ren, Global band convergence design for high-performance thermoelectric power generation in Zintls. *Science* **384**, 757–762 (2024).
19. Y. Xing, R. Liu, J. Liao, C. Wang, Q. Zhang, Q. Song, X. Xia, T. Zhu, S. Bai, L. Chen, A device-to-material strategy guiding the "double-high" thermoelectric module. *Joule* **4**, 2475–2483 (2020).
20. A. Mehdizadeh Dehkordi, M. Zebarjadi, J. He, T. M. Tritt, Thermoelectric power factor: Enhancement mechanisms and strategies for higher performance thermoelectric materials. *Mat. Sci. Eng. R. Rep.* **97**, 1–22 (2015).
21. A. Li, C. Hu, B. He, M. Yao, C. Fu, Y. Wang, X. Zhao, C. Felser, T. Zhu, Demonstration of valley anisotropy utilized to enhance the thermoelectric power factor. *Nat. Commun.* **12**, 5408 (2021).
22. B. Qin, L.-D. Zhao, Carriers: The less, the faster. *Mat. Lab* **1**, 220004 (2022).
23. A. Li, M. K. Brod, Y. Wang, K. Hu, P. Nan, S. Han, Z. Gao, X. Zhao, B. Ge, C. Fu, S. Anand, G. J. Snyder, T. Zhu, Opening the bandgap of metallic half-heuslers via the introduction of d–d orbital interactions. *Adv. Sci.* **10**, e2302086 (2023).
24. L. Xie, L. Yin, Y. Yu, G. Peng, S. Song, P. Ying, S. Cai, Y. Sun, W. Shi, H. Wu, N. Qu, F. Guo, W. Cai, H. Wu, Q. Zhang, K. Nielsch, Z. Ren, Z. Liu, J. Sui, Screening strategy for developing thermoelectric interface materials. *Science* **382**, 921–928 (2023).
25. W. Liu, S. Bai, Thermoelectric interface materials: A perspective to the challenge of thermoelectric power generation module. *J. Materiomics* **5**, 321–336 (2019).
26. J. Pei, B. Cai, H.-L. Zhuang, J.-F. Li, Bi_2Te_3-based applied thermoelectric materials: Research advances and new challenges. *Natl. Sci. Rev.* **7**, 1856–1858 (2020).
27. R. Cheng, H. Ge, S. Huang, S. Xie, Q. Tong, H. Sang, F. Yan, L. Zhu, R. Wang, Y. Liu, M. Hong, C. Uher, Q. Zhang, W. Liu, X. Tang, Unraveling electronic origins for boosting thermoelectric performance of p-type $(Bi,Sb)_2Te_3$. *Sci. Adv.* **10**, eadn9959 (2024).
28. Y. Li, F. Liu, B. Ying, J. Liu, Y. He, K. Liu, A. Li, Y. Wu, Z. Tang, P. Nan, B. Ge, C. Fu, T. Zhu, Grain recovery facilitated low-angle grain boundaries and texture for high-performance BiSbTe alloys. *Mater. Today Phys.* **49**, 101591 (2024).
29. X. Wu, Y. Lin, C. Liu, Y. Wang, H. Li, B. Ge, W. Liu, A high performance eco-friendly MgAgSb-based thermoelectric power generation device near phase transition temperatures. *Energ. Environ. Sci.* **17**, 2879–2887 (2024).
30. L. Wang, A. Li, J. Li, N. Kawamoto, D. H. Nguyen, T. Mori, Homogenizing composition to achieve high-performance Mg_3Bi_2-type thermoelectrics. *Nano Energy* **137**, 110797 (2025).
31. M. J. Kirkham, A. M. dos Santos, C. J. Rawn, E. Lara-Curzio, J. W. Sharp, A. J. Thompson, Ab initio determination of crystal structures of the thermoelectric material MgAgSb. *Phys. Rev. B* **85**, 144120 (2012).
32. H. Zhao, J. Sui, Z. Tang, Y. Lan, Q. Jie, D. Kraemer, K. McEnaney, A. Guloy, G. Chen, Z. Ren, High thermoelectric performance of MgAgSb-based materials. *Nano Energy* **7**, 97–103 (2014).
33. Z. Liu, J. Mao, J. Sui, Z. Ren, High thermoelectric performance of α-MgAgSb for power generation. *Energ. Environ. Sci.* **11**, 23–44 (2018).
34. P. Ying, X. Liu, C. Fu, X. Yue, H. Xie, X. Zhao, W. Zhang, T. Zhu, High performance α-MgAgSb thermoelectric materials for low temperature power generation. *Chem. Mater.* **27**, 909–913 (2015).
35. S. Y. Back, S. Meikle, T. Mori, Comprehensive study of α-MgAgSb: Microstructure, carrier transport properties, and thermoelectric performance under ball milling techniques. *J. Mater. Sci. Technol.* **227**, 57–66 (2025).
36. Y. Zheng, C. Liu, L. Miao, C. Li, R. Huang, J. Gao, X. Wang, J. Chen, Y. Zhou, E. Nishibori, Extraordinary thermoelectric performance in MgAgSb alloy with ultralow thermal conductivity. *Nano Energy* **59**, 311–320 (2019).
37. Z. Liu, Y. Wang, J. Mao, H. Geng, J. Shuai, Y. Wang, R. He, W. Cai, J. Sui, Z. Ren, Lithium doping to enhance thermoelectric performance of MgAgSb with weak electron–phonon coupling. *Adv. Energy Mater.* **6**, 1502269 (2016).
38. A. Li, L. Wang, J. Li, T. Mori, Global softening to manipulate sound velocity for reliable high-performance MgAgSb thermoelectrics. *Energ. Environ. Sci.* **17**, 8810–8819 (2024).
39. X. Zhang, H. Zhu, X. Dong, Z. Fan, Y. Yao, N. Chen, J. Yang, K. Guo, J. Hao, L. He, G. Li, H. Zhao, High-performance MgAgSb/$Mg_3(Sb,Bi)_2$-based thermoelectrics with $\eta = 12\%$ at $T \le 583$ K. *Joule* **8**, 3324–3335 (2024).
40. A. Li, L. Wang, J. Li, X. Wu, T. Mori, Self-optimized contact in air-robust thermoelectric junction towards long-lasting heat harvesting. *Nat. Commun.* **16**, 1502 (2025).
41. W. Zuo, H. Chen, Z. Yu, Y. Fu, X. Ai, Y. Cheng, M. Jiang, S. Wan, Z. Fu, R. Liu, G. Cheng, R. Xu, L. Wang, F. Xu, Q. Zhang, D. Makarov, W. Jiang, Atomic-scale interface strengthening unlocks efficient and durable Mg-based thermoelectric devices. *Nat. Mater.* **24**, 735–742 (2025).
42. Y. Huang, J. Lei, H. Chen, Z. Zhou, H. Dong, S. Yang, H. Gao, T.-R. Wei, K. Zhao, X. Shi, Intrinsically high thermoelectric performance in near-room-temperature α-MgAgSb materials. *Acta Mater.* **249**, 118847 (2023).
43. Z. Zhang, Y. Zhu, J. Ji, J. Zhang, H. Luo, C. Fu, Q. Li, M. Brod, G. J. Snyder, Y. Zhang, J. Yang, W. Zhang, Ag rearrangement induced metal-insulator phase transition in thermoelectric MgAgSb. *Mat. Today Phys.* **25**, 100702 (2022).
44. R. Chetty, J. Babu, T. Mori, Best practices for evaluating the performance of thermoelectric devices. *Joule* **8**, 556–562 (2024).
45. J. Sui, J. Shuai, Y. Lan, Y. Liu, R. He, D. Wang, Q. Jie, Z. Ren, Effect of Cu concentration on thermoelectric properties of nanostructured p-type $MgAg_{0.97-x}Cu_xSb_{0.99}$. *Acta Mater.* **87**, 266–272 (2015).
46. A. Duparchy, L. Millerand, J. Camut, S. Tumminello, H. Kamila, R. Deshpande, A. Cowley, E. Mueller, J. de Boor, Establishing synthesis–composition–property relationships for

enhanced and reproducible thermoelectric properties of MgAgSb. *J. Mater. Chem. A* **10**, 21716–21726 (2022).

47. Z. Liu, Y. Zhang, J. Mao, W. Gao, Y. Wang, J. Shuai, W. Cai, J. Sui, Z. Ren, The microscopic origin of low thermal conductivity for enhanced thermoelectric performance of Yb doped MgAgSb. *Acta Mater.* **128**, 227–234 (2017).
48. Y. Pan, Y. Qiu, I. Witting, L. Zhang, C. Fu, J.-W. Li, Y. Huang, F.-H. Sun, J. He, G. J. Snyder, C. Felser, J.-F. Li, Synergistic modulation of mobility and thermal conductivity in $(Bi,Sb)_2Te_3$ towards high thermoelectric performance. *Energ. Environ. Sci.* **12**, 624–630 (2019).
49. Y. Pei, X. Shi, A. LaLonde, H. Wang, L. Chen, G. J. Snyder, Convergence of electronic bands for high performance bulk thermoelectrics. *Nature* **473**, 66–69 (2011).
50. J. Sui, J. Li, J. He, Y.-L. Pei, D. Berardan, H. Wu, N. Dragoe, W. Cai, L.-D. Zhao, Texturation boosts the thermoelectric performance of BiCuSeO oxyselenides. *Energ. Environ. Sci.* **6**, 2916–2920 (2013).
51. H. Liu, X. Shi, F. Xu, L. Zhang, W. Zhang, L. Chen, Q. Li, C. Uher, T. Day, G. J. Snyder, Copper ion liquid-like thermoelectrics. *Nat. Mater.* **11**, 422–425 (2012).
52. J.-L. Mi, P.-J. Ying, M. Sist, H. Reardon, P. Zhang, T.-J. Zhu, X.-B. Zhao, B. B. Iversen, Elaborating the crystal structures of MgAgSb thermoelectric compound: Polymorphs and atomic disorders. *Chem. Mater.* **29**, 6378–6388 (2017).
53. L. Jiao, L. Xie, Y.-K. Zhu, L. Wang, Y. Sun, Y. Yu, A. Ivanova, V. Khovaylo, F. Guo, W. Cai, J. Sui, Z. Liu, Grain boundary segregation mediated highly stable and high performance nanostructured MgAgSb bulk thermoelectric materials. *Trans. Mater. Res.* **1**, 100016 (2025).
54. P. Ying, R. He, J. Mao, Q. Zhang, H. Reith, J. Sui, Z. Ren, K. Nielsch, G. Schierning, Towards tellurium-free thermoelectric modules for power generation from low-grade heat. *Nat. Commun.* **12**, 1121 (2021).
55. L. Wang, W. Zhang, S. Y. Back, N. Kawamoto, D. H. Nguyen, T. Mori, High-performance Mg_3Sb_2-based thermoelectrics with reduced structural disorder and microstructure evolution. *Nat. Commun.* **15**, 6800 (2024).
56. J. Li, R. Chetty, Z. Liu, W. Gao, T. Mori, Enhancing the thermoelectric performance of n-Type Mg_3Sb_2-based materials via ag doping. *Small* **21**, e2408059 (2025).
57. P. Ying, H. Reith, K. Nielsch, R. He, Geometrical optimization and thermal-stability characterization of Te-free thermoelectric modules based on MgAgSb/$Mg_3(Bi,Sb)_2$. *Small* **18**, 2201183 (2022).
58. L. Yin, F. Yang, X. Bao, W. Xue, Z. Du, X. Wang, J. Cheng, H. Ji, J. Sui, X. Liu, Y. Wang, F. Cao, J. Mao, M. Li, Z. Ren, Q. Zhang, Low-temperature sintering of Ag nanoparticles for high-performance thermoelectric module design. *Nat. Energy* **8**, 665–674 (2023).
59. G. Kresse, J. Furthmüller, Efficient iterative schemes for ab initio total-energy calculations using a plane-wave basis set. *Phys. Rev. B* **54**, 11169–11186 (1996).
60. G. Kresse, D. Joubert, From ultrasoft pseudopotentials to the projector augmented-wave method. *Phys. Rev. B* **59**, 1758–1775 (1999).
61. J. P. Perdew, K. Burke, M. Ernzerhof, Generalized gradient approximation made simple. *Phys. Rev. Lett.* **77**, 3865–3868 (1996).
62. F. Tran, P. Blaha, Accurate band gaps of semiconductors and insulators with a semilocal exchange-correlation potential. *Phys. Rev. Lett.* **102**, 226401 (2009).
63. V. Wang, N. Xu, J.-C. Liu, G. Tang, W.-T. Geng, VASPKIT: A user-friendly interface facilitating high-throughput computing and analysis using VASP code. *Comput. Phys. Commun.* **267**, 108033 (2021).

Acknowledgments: This work was carried out with center support from JSPS WPI Academy. **Funding:** This work was supported by the JST Mirai Program grant JPMJMI19A1 (to T.M.) **Author contributions:** Conceptualization: A.L., X. Wu, and T.M. Methodology: A.L., L.W., and T.M. Validation: A.L. and L.W. Formal analysis: A.L. and X. Wu. Investigation: A.L., L.W., J.L., and X.Wa. Resources: A.L. and L.W. Writing—original draft: A.L. Writing—review and editing: A.L., L.W., X. Wu, J.L., X.Wa., G.W., Z.H., and T.M. Visualization: A.L. Supervision: T.M. Project administration: T.M. Funding acquisition: T.M. **Competing interests:** T.M. and A.L. have filed one Japanese patent application (2024-111372) submitted by National Institute for Materials Science (Japan). The other authors declare that they have no competing interests. **Data and materials availability:** All data needed to evaluate the conclusions in the paper are present in the paper and/or the Supplementary Materials.

Submitted 25 March 2025
Accepted 2 June 2025
Published 4 July 2025
10.1126/sciadv.adx7115